Observation of three-state nematicity and domain evolution in atomically-thin antiferromagnetic $NiPS_3$

Qishuo Tan[1†], Connor A. Occhialini[2†], Hongze Gao[1], Jiaruo Li[2], Hikari Kitadai[1], Riccardo Comin[2*], and Xi Ling[1, 3, 4*]

[1] Department of Chemistry, Boston University, Boston, Massachusetts, 02215, USA.
[2] Department of Physics, Massachusetts Institute of Technology, Cambridge, Massachusetts, 02139, USA.
[3] Division of Materials Science and Engineering, Boston University, Boston, Massachusetts, 02215, USA.
[4] The Photonics Center, Boston University, Boston, Massachusetts, 02215, USA.

†These authors contributed equally to this work.
*To whom the correspondence should be addressed. Email address: rcomin@mit.edu; xiling@bu.edu

Keywords: van der Waals; 2D magnetic material; magnetic domains; spin detection; nickel phosphorus trisulfide

Abstract

Nickel phosphorus trisulfide ($NiPS_3$), a van der Waals two-dimensional antiferromagnet, has received significant interest for its intriguing properties in recent years. However, despite its fundamental importance in the physics of low-dimensional magnetism and promising potential for technological applications, the study of magnetic domains in $NiPS_3$ down to atomically thin is still lacking. Here, we report the layer-dependent magnetic characteristics and magnetic domains in $NiPS_3$ by employing linear dichroism spectroscopy, polarized microscopy, spin-correlated photoluminescence, and Raman spectroscopy. Our results reveal the existence of the paramagnetic-to-antiferromagnetic phase transition in bulk to bilayer $NiPS_3$ and evidence the role of stronger spin fluctuations in thin $NiPS_3$. Furthermore, our study identifies three distinct antiferromagnetic domains within atomically-thin $NiPS_3$ and captures the thermally-activated domain evolution. Our findings provide crucial insights for the development of antiferromagnetic spintronics and related technologies.

Antiferromagnets (AFMs) are materials in which magnetic moments align in long-range order yet with zero net magnetic moment below a critical transition temperature. Historically overshadowed by the prominence of ferromagnets, AFMs were once labelled as "interesting but useless" for quite a long time[1]. Back then, the detection of antiferromagnetic order were one of the central challenges. Further, one could only manipulate these materials by very strong magnetic fields on the order of several tesla, thus limiting the ability to control antiferromagnetic order. Nowadays, the advancement of technology has ushered in new methodologies for studying AFMs, including those leveraging light-matter interactions[2,3]. Revealed through the combination of conventional and new approaches, intrinsic strengths of AFMs such as their terahertz spin resonance, multilevel states and absence of stray fields, have positioned them as promising candidates for next-generation spintronics[4,5]. As a crucial factor affecting the performance of applications, the study of antiferromagnetic domains has thus garnered considerable attention[6–8], especially in two dimensional (2D) region[9–11].

Nickel phosphorus trisulfide ($NiPS_3$), an emerging van der Waals (vdW) 2D antiferromagnetic material from the family of transition metal trichalcogenides, offers an exceptional platform for investigating the electronic and magnetic properties of strongly correlated 2D systems, such as magnetic dynamics[12–14], phonon-magnon coupling[15,16], spin-correlated emission[17–20], and inelastic scattering/transition from *d-d* excitations[21–23]. However, despite these interesting spin-correlated phenomena and their promise for AFMs-based spintronics, the investigation of magnetic domains and their evolution with temperature especially in atomically-thin $NiPS_3$ is still lacking.

In this study, we use optical linear dichroism (LD) to probe the thickness-dependent antiferromagnetism and magnetic domains in $NiPS_3$ down to atomically-thin layers combined with polarized microscopy, PL, and Raman spectroscopy. Our measurements from pentalayer (5 L) to bilayer (2 L) $NiPS_3$ reveal a trend of decreasing magnetic phase transition temperature and stronger spin fluctuation. Notably, no LD signals are detected from monolayer $NiPS_3$, strongly evidencing the absence of long-range magnetic ordering. Moreover, a three-state nematicity related to the underlying zig-zag antiferromagnetic order is observed in atomically thin $NiPS_3$ by angular-dependent LD measurements, further supported through polarized exciton emission and Raman spectroscopy. The evolution of magnetic domains with increasing temperature in 2 L $NiPS_3$ is also captured, demonstrating a process of thermally activated domain wall motion.

Bulk $NiPS_3$ has a monoclinic stacking configuration within space group $C2/m$ with weak interlayer coupling[15,24]. As shown in Fig. 1a, Ni atoms arranged in a hexagonal lattice establish an in-plane zigzag antiferromagnetic order within each layer at temperature below its Néel temperature (T_N). Previous neutron scattering measurements on bulk $NiPS_3$ show that spins of Ni atoms align either parallel or anti-parallel along *a* axis in the *ab* plane[25,26], and interlayer spins are coupled ferromagnetically. As for $NiPS_3$ flakes, there would be three possible in-plane zigzag antiferromagnetic orders as depicted in Fig. 1b, which indicates the formation of three-state Potts nematic order (Z_3)[27] that is similar to monoclinic $FePS_3$[28]. To investigate the magnetic properties in $NiPS_3$ flakes, we mechanically exfoliated them from bulk single crystal onto silicon substrates (e.g., Fig. S1a). The spin-correlated sharp PL peak of 1.476 eV, and the characteristic Raman peaks are observed (Fig. S1b-c), indicating that samples are in high-quality.

The measurement of linear dichroism (LD) whether employing laser or X-ray light as an excitation, offers a potent technique for probing the symmetry breaking in 2D materials[10,29–32]. Figure 1c illustrates the experimental setup for the reflective LD measurements, with more details in the Methods section. Figure 1d shows the temperature-dependent LD spectra of a thick $NiPS_3$ sample (Fig. S1a), with prominent signals arising while the energies are in resonance

with the charge-transfer exciton[33] at around 1.9-2.1 eV and the spin-correlated exciton[19] at around 1.5 eV. With increasing temperature, these signals diminish until vanishing above T_N. We extract the LD signals at the energy of 2.05 eV and plot the temperature dependence in Fig. 1e. The temperature-dependent LD intensity is fitted using the formula

$$\mathrm{LD}(T) \sim \left(1 - \frac{T}{T_N}\right)^{2\beta_{LD}} \quad (1),$$

where T_N is the transition temperature, and β_{LD} is the critical exponent describing the evolution of the order parameter through the magnetic phase transition[34,35]. Thick $NiPS_3$ shows a T_N of 157 K and a β_{LD} of 0.25.

We further use a cross-polarized microscopy to characterize the magnetic domains, where an incident linearly polarized light impinges on the sample and the reflected light is detected. Due to the birefringence effect induced by magnetization vector, the polarization of the reflected light would depend on magnetic domains, resulting in a contrast difference for magnetic domains by detuning the incident and reflected light polarization[36]. Figure 1f shows the polarized microscopy image of the thick $NiPS_3$ sample measured at 5 K, wherein the contrast difference signifies the presence of two distinct domains, i.e. the major Domain_1 outlined by green dashed lines, and the smaller Domain_2 outlined by blue dashed lines. As we increase the temperature, these domains vanish when T is higher than T_N of 157 K (Fig. S2), indicating their magnetic origin. The coexistence of antiferromagnetic domains is also substantiated through LD mapping within the same area (Fig. 1g). To probe the direction of the Néel vector, we measure the angular-dependent LD on each mono-domain region. Since the light absorption parallel to Néel vector is stronger than that perpendicular to Néel vector for $NiPS_3$ [19], the negative maxima of reflective LD results showcase the direction of Néel vector, i.e., the orientation of the zig-zag antiferromagnetic ordering. From the angular-dependent LD results shown in Fig. 1h, the Néel vector of Domain_1 is along 0°, but it is along 60° (-120°) for Domain_2. This angular discrepancy of 120° for the antiferromagnetic ordering matches with the three-state nematicity shown in Fig. 1b. Furthermore, given the report that the spin-correlated PL is perpendicular to the Néel vector[19], we also conduct PL mapping and angular-dependent PL measurements on the same area (Fig. S3), yielding outcomes that align with the aforementioned techniques. These two domains related by 120° in their Néel vectors implies the existence of a third domain which are observed in atomically-thin samples presented in the following.

To investigate the antiferromagnetism and domains further in atomically thin samples, we extend the LD measurements to $NiPS_3$ flakes from 1 L to 5 L. Figure 2a presents the optical image of the $NiPS_3$ flakes ranging from 1 L to 5 L determined by the optical contrasts (Fig. 2b)[37]. Figure 2c shows the layer-dependent LD results measured at 1.75 K, revealing robust signals from 2 L to 5 L, whereas no signals from the monolayer are observed. The layer-dependent LD intensity is summarized in Fig. 2e, showing a nonlinear increase with the increase of the layer number likely due to interference effects. We further performed the temperature-dependent LD measurements on these regions (Fig. 2d). With the increase of temperature, decreasing LD signals are observed for 2 L to 5 L samples, which eventually vanishes above their respective Néel temperatures. For monolayer sample, no visible signal or phase transition are observed. Additional LD spectroscopy and Raman measurements are shown in Fig. S4 and Fig. S5, supporting the suppression of magnetic ordering in monolayer $NiPS_3$. The fitted layer-dependent values of T_N and β_{LD} by equation (1) are summarized in Fig. 2f and 2g, respectively. Evidently, the transition temperature decreases from 154 K for 5 L to 121 K for 2 L. This conspicuous dimensional effect of lower T_N for thinner sample is also observed in other 2D AFMs such as $MnPS_3$ [38–40], $FePS_3$ [41–43], $MnPSe_3$ [11,44]. In addition, the critical exponent β_{LD} increases from 0.25 for 5 L to 0.35 for 2 L. The β_{LD} of 0.25 for 5 L and thick $NiPS_3$ aligns well with previous report[19] and reflects the universal signature of 2D XY magnetic system[45]. However, as $NiPS_3$

becomes thinner, a larger critical exponent is observed meaning a quicker decrease of magnetization with rising temperature. This may be induced by a weaker easy-plane-like anisotropy, and implies stronger spin fluctuation in all three dimensions for thinner $NiPS_3$ [15].

We then apply the angular LD measurements to study magnetic domains of atomically-thin $NiPS_3$. Figure 3a shows the optical image of a four-layer $NiPS_3$ flake with edges delineated by black dashed lines. LD mappings with the incident laser polarization at 0°, 60°, 90°, 120°, 150° and 210° are performed at 4 K (Fig. 3b-d and Fig. S6), where the LD signal flip from negative maximum to positive maximum when rotating the incident laser polarization by 90°, indicating the existence of the magnetic domain. For better visualization, each of the mono-domain regions is outlined in green, blue, and red in the corresponding Fig. 3b, c, and d. The angular-dependent LD of each highlighted mono-domains is measured and shown in Fig. 3e. It clearly shows that the Néel vector aligns at 0°, 60° (-120°), and 120° for Domain_1, Domain_2, and Domain_3, respectively, demonstrating the observation of the three-state nematicity as represented by the cartoons in Fig. 3g. Interestingly, the edge of the sample shows a new LD pattern different from any domain of the inner region (Fig. S6b) that may result from local structure distortion[46,47], which falls beyond the scope of this study. We further perform the angular-dependent PL measurements on the three observed domains. Figure 3f shows the intensity polar plots of the sharp PL emission at 1.476 eV for each magnetic domain, presenting signals reach a maximum when the collection polarization is along 90°, 150°, and 210° for the three domains, respectively. As the sharp PL emission is spin-correlated and its polarization is perpendicular to the Néel vector[19,48], these results suggest that the Néel vector of Domain_1, Domain_2 and Domain_3 is along 0°, 60° (-120°), and 120°, respectively, which is consistent with the LD measurements, further confirming the existence of the three-state nematicity. Polarized Raman measurements (Fig. S7) reveal that the major domain (i.e. Domain_1) of the 4 L $NiPS_3$ possesses the antiferromagnetic order along the *a*-axis[48]. Similarly, the three-state nematicity is also observed in a thinner 2-3 L flake as shown in Fig. S8-10.

To investigate the magnetic domain evolution, we perform LD mapping on the 2-3 L $NiPS_3$ sample with variable temperature in the range of 2 K to 175 K. Figure 4a shows the representative domain evolution, with additional results presented in Fig. S11. All three domains are observed in both the 2 L and 3 L regions at 2 K. For the 2 L flake, the major domain is Domain_2, accompanied by a small Domain_1 situated in the middle, while Domain_3 remains pinned near the right edge. With increasing temperature, the small Domain_1 within the 2 L region starts to grow from its edge, extending towards the right section of the flake. As temperature reaches 105 K, the entire right section of the 2 L region transitions into mono-Domain_1 completely. When temperature approaches to T_N, specifically 121 K for 2 L sample gained from the layer-dependent LD measurements (Fig. 2f), LD signals dramatically drop until they vanish above T_N. Figure 4b shows the temperature-dependent LD intensity measured at the labelled 2 L position by black dots in Fig. 4a, revealing a sign change of the LD signal from positive to negative, signifying a thermal-induced change of the local magnetic domain. The orientation of the antiferromagnetic ordering before and after the domain flip is confirmed by angular-dependent LD measurements on the labelled 2 L position (Fig. 4c). We observe that the LD negative maximum changes from along 60° (-120°) at 2 K to along 0° at 85 K, illustrating the transition from Domain_2 to Domain_1. Similarly, the left section of the 2 L flake change from Domain_2 to Domain_3, possibly originating from the domain wall motion of Domain_3 from the adjacent 3 L flake. In contrast to the thermally-activated domain evolution in 2 L region, magnetic domains in the 3 L region and the thick sample exhibit no change across various temperatures until they disappear above T_N (also see Fig. S2 for the thick sample).

We attribute the origin of the magnetic domain evolution in 2 L $NiPS_3$ to the competition

between local strain and thermal fluctuation. Notably, we observe that upon conducting repeated LD mapping in various thermal cycles, the domain distribution remains unchanged at 2 K, which implies that domains are not degenerate but pinned by local effects such as strain[28]. This notion is reinforced by evidence that the residual LD signals at $T = 175$ K (considerably higher than the T_N of bulk $NiPS_3$) can depict the possible strain in the sample and match with the domain structure observed at 2 K (Fig. S11), which implies that strain defines the domain distribution as illustrated in Fig. 4d. As for substantially thicker bulk samples, these local effects might be imperceptible in comparison to the stabilization of monoclinic stacking, resulting in the antiferromagnetic order along the crystalline *a*-axis measured by magnetometry and neutron scattering[25]. In the case of atomically-thin $NiPS_3$ (e.g. 3 L sample), strain plays significant role to overcome the formation energy differences among these three domains, leading to the observation of three-state nematicity (Fig. 4d). Nevertheless, the high stability of antiferromagnetism leads to the instant formation of magnetic domains restricted by strain at $T < T_N$, thus no domain flip is observed in 3 L and thicker $NiPS_3$. However, when $NiPS_3$ goes down to 2 L, the spin fluctuation is stronger so adequate thermal fluctuation would overcome the energy barrier of these domains, resulting in a non-stable domain distribution at high temperature (Fig. 4e). As the temperature drops considerably below T_N, thermal fluctuation becomes weak and allows the strain-defined domains to construct until reaching the stable domain distribution. This impact of thermal fluctuation on 2 L $NiPS_3$ is reaffirmed by the varying domain distributions in different thermal cycles (Fig. S12).

In summary, our investigations on thickness-dependent antiferromagnetism in $NiPS_3$ reveal robust magnetic phase transitions down to bilayer limit, the lower magnetic phase transition temperature and stronger spin fluctuation from pentalayer to bilayer, and the emergence of three-state nematicity. Additionally, thermally-activated domain wall movement due to strong spin fluctuation in bilayer $NiPS_3$ is observed, imparting fundamental knowledge pivotal for future research endeavors including strategies for manipulating the antiferromagnetic behavior. Our study provides significant insights to the advancement of next-generation 2D antiferromagnetic spintronics.

Supporting Information Additional experimental results, including the characterization of $NiPS_3$ using Raman and PL spectroscopy; the domain observation by polarized microscopy and LD/PL mapping; the analysis of layer-dependent Raman, PL and LD; the observation of magnetic domain evolution and varying domain distribution.

Methods

$NiPS_3$ Crystal Synthesis. $NiPS_3$ single crystals were synthesized following our previous work[19]. Thin flakes were obtained by mechanical exfoliation and their thicknesses were determined by optical microscopy (Nikon DS-Ri2). Samples then were loaded into a closed-cycle optical cryostat by Montana Instruments or Quantum Design for all the temperature-dependent measurements.

PL and Raman spectroscopy measurements. PL and Raman measurements were conducted by using a confocal microscope spectrometer (Horiba LabRAM HR Evolution) with a $\times 50$ objective and 532 nm laser excitation. Signals were dispersed by a 600 gr/mm grating for PL, and by a 1800 gr/mm grating for Raman, detected with a liquid nitrogen cooled charge-coupled device (CCD) camera. The polarization angle-resolved PL measurements were performed by adding a linearly polarizer on the collective path. Co-linearly polarized Raman were conducted by adding a half-wave plate before the objective.

Linear dichroism measurements. A photo-elastic modulator (PEM; PEM-100, Hinds Instruments) was used on the incident path of the optical setup. A supercontinuum laser (NKT Photonics) resolved by a monochromater (resolution $\sim$ 5 meV) was used as excitation, which was focused onto samples using a $\times 50$ objective. The back-scattered light was collected by the same objective and measured by an amplified photodiode (ThorLabs PDA100A2), in which the output was connected to a lock-in amplifier (Stanford Instruments SR865A) referenced to the second harmonic of the fundamental PEM frequency f = 50 kHz. The beam incident on the PEM was prepared with linear polarization making an angle of 45° with respect to the PEM fast axis and the amplitude was modulated with a mechanical chopper at frequency of 578 Hz. The PEM retardance was set to 0.5λ to modulate the incident polarization. The total reflectance of the sample as a normalization, was monitored by a second lock-in amplifier referenced to the chopping frequency. A zero-order half-wave plate for changing the polarization states of the incident light after PEM was used and placed before the objective. All LD measurements except the LD spectra were conducted with the excitation wavelength of 633 nm.

Polarized microscopy. A broadband visible LED light, and linearly polarizers on both the input and output paths were used in a reflection geometry, with the images captured by a monochrome camera (ThorLabs CS165MU).

Data availability. Data that support the study in this article are available from the corresponding authors on reasonable request.

Acknowledgements. This material is based upon work supported by the National Science Foundation (NSF) under Grant No. 1945364. Q.T. acknowledges the support of the Laursen Graduate Research Award from Department of Chemistry at Boston University. H.G. acknowledges the support of BUnano fellowship from Boston University Nanotechnology Innovation Center. X.L. acknowledges the membership of the Photonics Center at Boston University. Work done by X.L. is also supported by the U.S. Department of Energy (DOE), Office of Science, Basic Energy Science (BES) under Award No. DE-SC0021064. Work at MIT (C.A.O., J.L., and R.C.) was supported by the U.S. Department of Energy, Office of Science National Quantum Information Science Research Center's Co-design Center for Quantum Advantage (C2QA) under contract number DE-SC0012704 (sample fabrication and optical characteriza-

tion). The cryomagnet used in this work (OptiCool, Quantum Design) was acquired with support from the Air Force Office of Scientific Research under the Defense University Research Instrumentation Program (DURIP) grant FA9550-22-1-0130.

Author contributions. Q.T., C.A.O., R.C. and X.L. conceived the project. Q.T., H.G., and H.K. synthesized and characterized the $NiPS_3$ crystals. Q.T., C.A.O., and J.L. performed the optical measurements supervised by R.C. and X.L. Q.T. and C.A.O. performed the data analysis and interpretation. Q.T. and X.L. wrote the manuscript with assistance of all authors.

Competing interests. The authors declare no competing interests.

References

[1] Néel, L. Magnetism and the local molecular field. *Nobel Lectures, Physics 1963-1970* (1970).

[2] Gibertini, M., Koperski, M., Morpurgo, A. F. & Novoselov, K. S. Magnetic 2D materials and heterostructure. *Nat. Nanotechnol.* **14**, 408–419 (2019).

[3] Gong, C. & Zhang, X. Two-dimensional magnetic crystals and emergent heterostructure devices. *Science* **363**, eaav4450 (2019).

[4] Jungwirth, T., Marti, X. & Wunderlich, J. Antiferromagnetic spintronics. *Nat. Nanotechnol.* **11**, 231–241 (2016).

[5] Němec, P., Fiebig, M., Kampfrath, T. & Kimel, A. Antiferromagnetic opto-spintronics. *Nat. Phys.* **14**, 229–241 (2018).

[6] Cheong, S. W., Fiebig, M., Wu, W., Chapon, L. & Kiryukhin, V. Seeing is believing: visualization of antiferromagnetic domains. *npj Quantum Mater.* **5**, 3 (2020).

[7] Hedrich, N. *et al.* Nanoscale mechanics of antiferromagnetic domain walls. *Nat. Phys.* **17**, 574–577 (2021).

[8] Krizek, F. *et al.* Atomically sharp domain walls in an antiferromagnet. *Sci. Adv.* **8**, eabn3535 (2022).

[9] Ni, Z. *et al.* Direct imaging of antiferromagnetic domains and anomalous layer-dependent mirror symmetry breaking in atomically thin $MnPS_3$. *Phy. Rev. Lett.* **127**, 187201 (2021).

[10] Zhang, Q. *et al.* Observation of giant optical linear dichroism in a zigzag antiferromagnet $FePS_3$. *Nano. Lett.* **21**, 6938–6945 (2021).

[11] Ni, Z. *et al.* Imaging the néel vector switching in the monolayer antiferromagnet $MnPSe_3$ with strain-controlled ising order. *Nat. Nanotechnol.* **16**, 782–787 (2021).

[12] Afanasiev, D. *et al.* Controlling the anisotropy of a van der waals antiferromagnet with light. *Sci. Adv.* **7**, eabf3096 (2021).

[13] Belvin, C. A. *et al.* Exciton-driven antiferromagnetic metal in a correlated van der waals insulator. *Nat. Commun.* **12**, 4837 (2021).

[14] Mehlawat, M. *et al.* Low-energy excitations and magnetic anisotropy of the layered van der waals antiferromagnet $Ni_2P_2S_6$. *Phys. Rev. B* **105**, 214427 (2022).

[15] Kim, K. *et al.* Suppression of magnetic ordering in XXZ-type antiferromagnetic monolayer $NiPS_3$. *Nat. Commun.* **10**, 345 (2019).

[16] Muhammad, Z. *et al.* Anisotropic phonon and magnon vibration and gate-tunable optoelectronic properties of nickel thiophosphite. *2D Mater.* **10**, 025001 (2023).

[17] Kang, S. *et al.* Coherent many-body exciton in van der waals antiferromagnet $NiPS_3$. *Nature* **583**, 785–789 (2020).

[18] Hwangbo, K. *et al.* Highly anisotropic excitons and multiple phonon bound states in a van der waals antiferromagnetic insulator. *Nat. Nanotechnol.* **16**, 655–660 (2021).

[19] Wang, X. *et al.* Spin-induced linear polarization of photoluminescence in antiferromagnetic van der waals crystals. *Nat. Mater.* **20**, 964–970 (2021).

[20] Jana, D. *et al.* Magnon gap excitations and spin-entangled optical transition in the van der waals antiferromagnet $NiPS_3$. *Phys. Rev. B* **108**, 115149 (2023).

[21] Wang, X. *et al.* Electronic Raman scattering in the 2D antiferromagnet $NiPS_3$. *Sci. Adv.* **8**, eabl7707 (2022).

[22] Ergeçen, E. *et al.* Magnetically brightened dark electron-phonon bound states in a van der waals antiferromagnet. *Nat. Commun.* **13**, 98 (2022).

[23] Tan, Q. *et al.* Charge-transfer-enhanced *d–d* emission in antiferromagnetic $NiPS_3$. *Appl. Phys. Rev.* **9**, 041406 (2022).

[24] Du, K. *et al.* Weak van der waals stacking, wide-range band gap, and raman study on ultrathin layers of metal phosphorus trichalcogenides. *ACS Nano* **10**, 1738–1743 (2016).

[25] Wildes, A. *et al.* Magnetic structure of the quasi-two-dimensional antiferromagnet $NiPS_3$. *Phys. Rev. B* **92**, 224408 (2015).

[26] Wildes, A. R. *et al.* Magnetic dynamics of $NiPS_3$. *Phys. Rev. B* **106**, 174422 (2022).

[27] Little, A. *et al.* Three-state nematicity in the triangular lattice antiferromagnet $Fe_{1/3}NbS_2$. *Nat. Mater.* **19**, 1062–1067 (2020).

[28] Ni, Z., Huang, N., Haglund, A. V., Mandrus, D. G. & Wu, L. Observation of giant surface second-harmonic generation coupled to nematic orders in the van der waals antiferromagnet $FePS_3$. *Nano. Lett.* **22**, 3283–3288 (2022).

[29] Zhang, H. *et al.* Cavity-enhanced linear dichroism in a van der waals antiferromagnet. *Nat. Photon.* **16**, 311–317 (2022).

[30] Song, Q. *et al.* Evidence for a single-layer van der waals multiferroic. *Nature* **602**, 601–605 (2022).

[31] Occhialini, C. A. *et al.* Spontaneous orbital polarization in the nematic phase of FeSe. *Nat. Mater.* **22**, 985–991 (2023).

[32] Lee, Y. *et al.* Giant magnetic anisotropy in the atomically thin van der waals antiferromagnet $FePS_3$. *Adv. Electron. Mater.* **9**, 2200650 (2023).

[33] Kim, S. *et al.* Charge-spin correlation in van der waals antiferromagnet $NiPS_3$. *Phys. Rev. Lett.* **120**, 136402 (2018).

[34] Ferre, J. & Gehring, G. A. Linear optical birefringence of magnetic crystals. *Rep. Prog. Phys.* **47**, 513–611 (1984).

[35] Taroni, A., Bramwell, S. T. & Holdsworth, P. C. W. Journal of physics: Condensed matter universal window for two-dimensional critical exponents. *J. Phys.: Condens. Matter* **20**, 275233 (2008).

[36] Xu, J. *et al.* Imaging antiferromagnetic domains in nickel oxide thin films by optical birefingence effect. *Phys. Rev. B* **100**, 134413 (2019).

[37] Kuo, C. *et al.* Exfoliation and Raman spectroscopic fingerprint of few-layer $NiPS_3$ van der waals crystals. *Sci. Rep.* **6**, 20904 (2016).

[38] Kim, K. *et al.* Antiferromagnetic ordering in van der waals 2D magnetic material $MnPS_3$ probed by Raman spectroscopy. *2D Mater.* **6**, 041001 (2019).

[39] Sun, Y. J., Tan, Q. H., Liu, X. L., Gao, Y. F. & Zhang, J. Probing the magnetic ordering of antiferromagnetic $MnPS_3$ by Raman spectroscopy. *J. Phys. Chem. Lett.* **10**, 3087–3093 (2019).

[40] Long, G. *et al.* Persistence of magnetism in atomically thin $MnPS_3$ crystals. *Nano. Lett.* **20**, 2452–2459 (2020).

[41] Lee, J. U. *et al.* Ising-type magnetic ordering in atomically thin $FePS_3$ crystals. *Nano. Lett.* **16**, 7433–7438 (2016).

[42] Wang, X. *et al.* Raman spectroscopy of atomically thin two-dimensional magnetic iron phosphorus trisulfide ($FePS_3$) crystals. *2D Mater.* **3**, 031009 (2016).

[43] Zhang, X. X. *et al.* Spin dynamics slowdown near the antiferromagnetic critical point in atomically thin $FePS_3$. *Nano. Lett.* **21**, 5045–5052 (2021).

[44] Liu, P. *et al.* Exploring the magnetic ordering in atomically thin antiferromagnetic $MnPSe_3$ by Raman spectroscopy. *J. Alloys Compd.* **828**, 154432 (2020).

[45] Bramwell, S. T. & Holdsworth, P. C. W. Magnetization and universal sub-critical behaviour in two-dimensional XY magnets. *J. Phys. Condens. Matter* **5**, L53–L59 (1993).

[46] Bao, W. *et al.* Visualizing nanoscale excitonic relaxation properties of disordered edges and grain boundaries in monolayer molybdenum disulfide. *Nat. Commun.* **6**, 7993 (2015).

[47] Wang, X., Mao, N., Luo, W., Kitadai, H. & Ling, X. Anomalous phonon modes in black phosphorus revealed by resonant raman scattering. *J. Phys. Chem. Lett.* **9**, 2830–2837 (2018).

[48] Kim, D. S. *et al.* Anisotropic excitons reveal local spin chain directions in a van der waals antiferromagnet. *Adv. Mater.* **35**, 19 (2023).

Figures

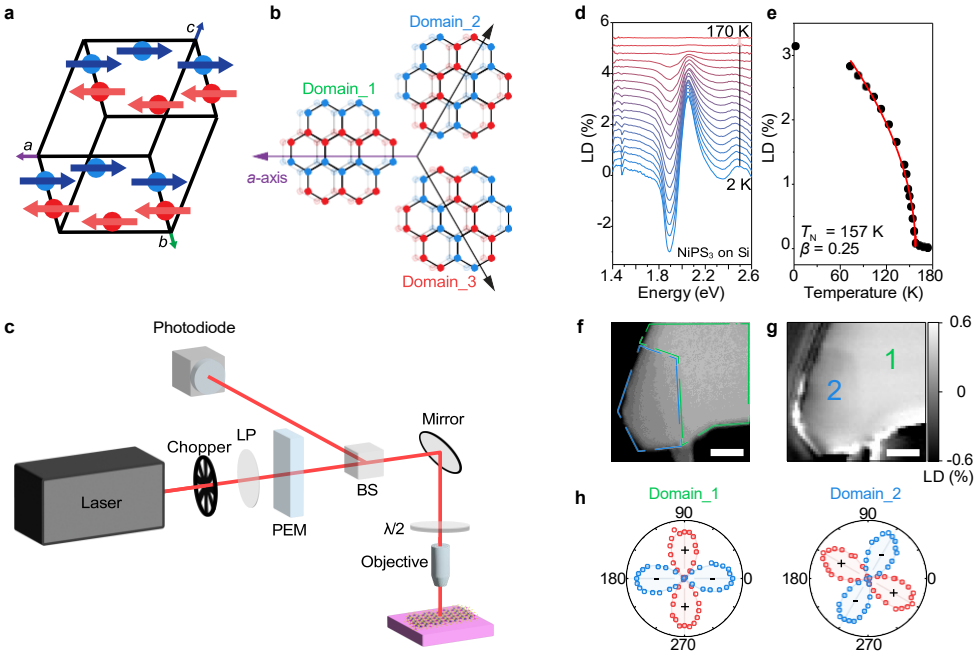

Fig. 1. Magnetic structure and detection of $NiPS_3$. **a**, Schematic of the spin structure on Ni atoms of $NiPS_3$. **b**, Three-state nematicity formed by zigzag antiferromagnetic orders. The spin direction up and down is represented by blue and red circles. **c**, Experimental setup for linear dichroism measurement. LP: linear polarizer, PEM: photo-elastic modulator, BS: beam splitter, $\lambda/2$: half-wave plate. **d**, Temperature-dependent LD spectra of a thick flake. **e**, Extracted LD values at the photo energy of 2.05 eV from **d**. The red line is the fitting using the formula $\mathrm{LD}(T) \sim \left(1 - \frac{T}{T_N}\right)^{2\beta_{LD}}$, where T_N = 157 K, and β_{LD} = 0.25. **f**, Polarized microscopy image and **g**, LD mapping of the same thick sample at 5 K, confirming the same two magnetic domains. Domain_1 and Domain_2 are labelled by green and blue dashed lines/numbers in **f**/**g**, respectively. Scale bar: 5 μm. **h**, Angular-dependent LD results of the thick sample on the two domain regions.

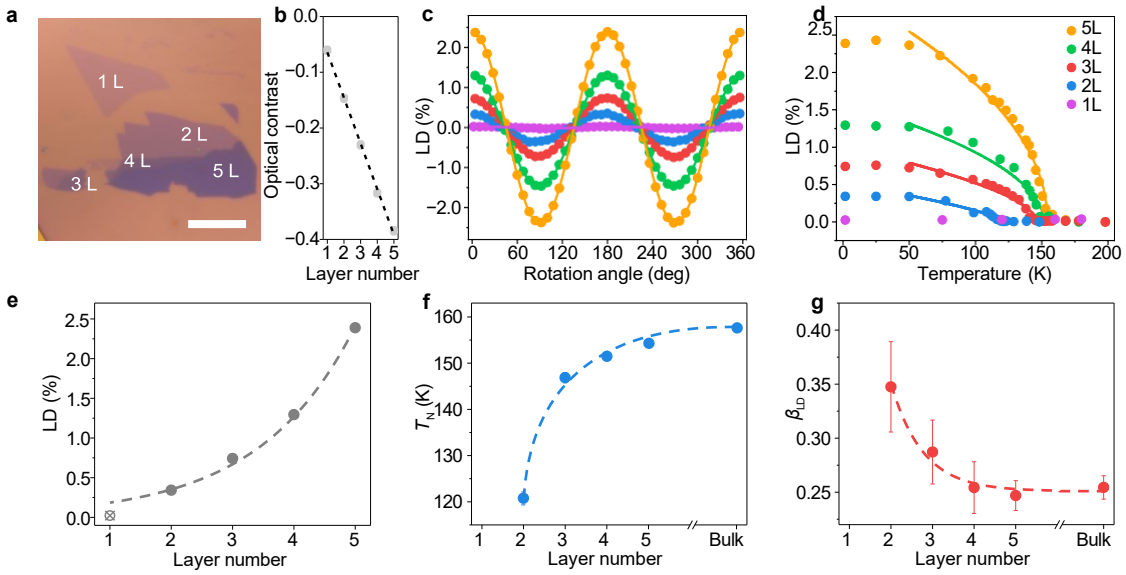

Fig. 2. Thickness-dependent magnetism of $NiPS_3$. **a**, Optical image of exfoliated $NiPS_3$ flakes with the layer number indicated. Scale bar: 10 μm. **b**, Optical contrast in red channel of the sample with different numbers of layers. **c**, Layer-dependent LD results measured at 1.8 K. **d**, Temperature-dependent LD results for 1-5 L $NiPS_3$ samples. Lines are the fitting using the formula, $\mathrm{LD}(T) \sim \left(1 - \frac{T}{T_N}\right)^{2\beta_{LD}}$, where T_N is the transition temperature, and β_{LD} is the critical exponent. **e**, Layer-dependent LD intensity acquired from measurement at 1.8 K. **f**, Layer-dependent transition temperature, T_N. **g**, Layer-dependent critical exponent, β_{LD}. Dash lines in **e**, **f**, and **g** are guides to the eye.

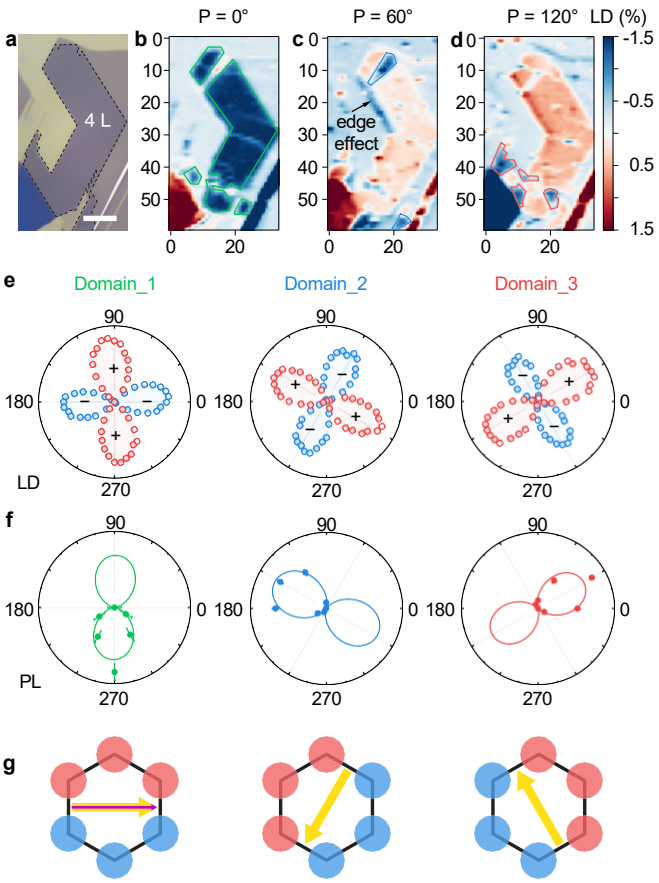

Fig. 3. Three-state nematicity in a four-layer $NiPS_3$. a, Optical image of 4 L $NiPS_3$ flake outlined by black dashed lines. Scale bar: 10 μm. **b-d**, LD intensity mapping on the same region in **a** with the incident laser polarization (P) at 0°, 60° and 120°. Domain_1, Domain_2, Domain_3 are outlined by green, blue, and red lines, respectively. **e**, Angular-dependent LD results in 4 L $NiPS_3$ on three domain regions. **f**, PL intensity as a function of the collection polarization. **g**, Schematics of three magnetic domains formed by zigzag order. Red and blue circles represent opposite in-plane spin directions on Ni atoms. Yellow arrows and purple arrow indicate the Néel vectors and the *a*-axis of the sample, respectively. All measurements are done at 4 K.

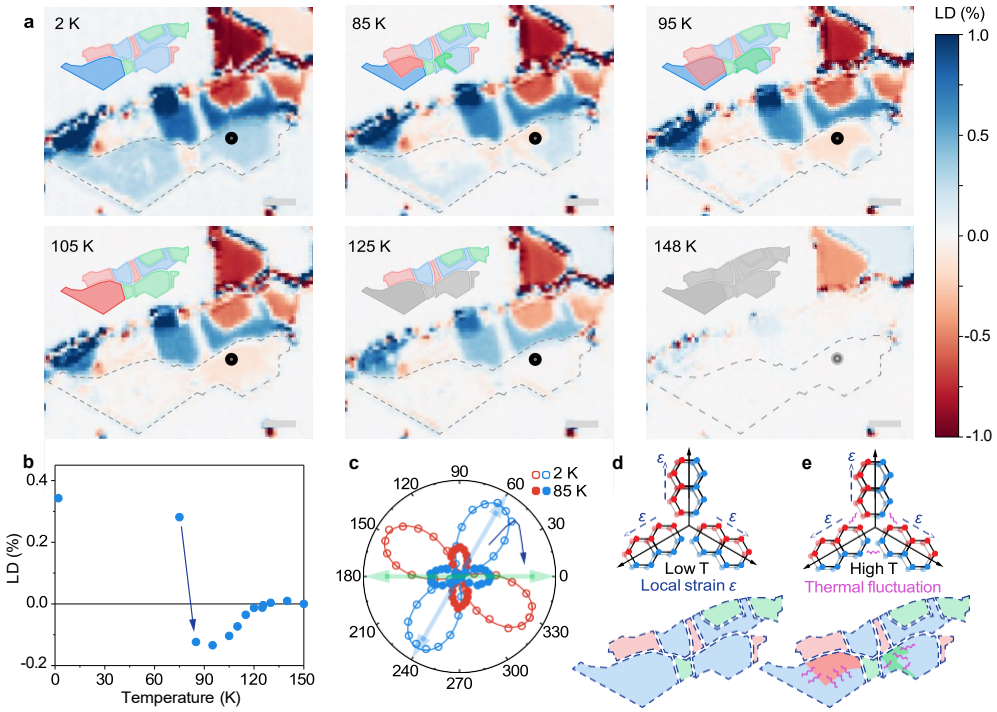

Fig. 4. Magnetic domain evolution of $NiPS_3$ with varying temperature. a, LD mapping images taken on an atomically-thin $NiPS_3$ flake from 2 K to 148 K. Signals measured at 175 K are subtracted as background. The inset cartoons picture the magnetic Domain_1, Domain_2, Domain_3 in green, blue, and red, respectively. When temperature is higher than T_N, LD signals disappear and is represented in grey color. The dashed lines depict the 2 L $NiPS_3$ region. The labelled position by the black dots are tracked by angular-dependent LD measurements. Scale bar: 10 μm. **b**, Temperature-dependent LD intensity for the labelled position of 2 L $NiPS_3$ in **a**. The sign change from positive to negative of LD intensity implies a magnetic domain flipping. **c**, Angular-dependent LD results on the labelled position in **a** at 2 K and 85 K. Green and blue arrows show the direction of the Néel vector. **d**, Mechanism of the domain evolution. Stable magnetic domain distribution confined by local strain is formed at low temperature. At high temperature, the thermal fluctuation provides sufficient energy for 2 L $NiPS_3$ to enable the domain flip.

For Table of Contents Only.